ISSN 2304-6295

Optimal Shape of Arch Concrete Block Bridge

Tyukalov, Yury Yakovlevich[1*]

[1]Vyatka State University, Kirov, Russian Federation
Correspondence: * email yutvgu@mail.ru; contact phone +79128218977

Keywords:

Arch bridge; Finite element method; Concretes; Optimal shape; Numerical methods; Cracks

Abstract:

The object of research is arched bridges made of concrete blocks backfilled with soil. The aim of the study was to develop a technique for determining the arch bridge's optimal shape in order to ensure the required size of the compressed cross-sectional zone at any automobile load position. The calculation takes into account the horizontal and vertical pressure of the backfill soil and the arch dead weight. The concrete blocks can have variable heights. **Method.** To solve the problem in a physically nonlinear formulation, the stepwise loading method and the possible stress states principle in increments were used. The solution was constructed by the finite element method based on piecewise constant approximations of the moments and forces. The nodes equilibrium equations obtained using the possible displacements principle are added to the additional energy functional written in increments form. The nodes vertical and horizontal displacements are accepted as possible displacements. When determining the required dimensions of the arch, the automobile load all possible positions are considered. **Results.** The optimum geometric parameters have been determined for an arch bridge with a span of 12 meters. The destructive automobile load value is determined**.** For the design load, the obtained internal moments and forces are compared with the ones calculated by the program based on the finite element method in displacements.

1 Introduction

Arched concrete and reinforced concrete structures with soil backfill are widely used for bridge crossings and overpasses. Such structures are easy manufactured and economical. Currently, the finite element method is used to calculate arch structures, as well as various analytical and numerical methods. In article [1] proposes an analytical method for determining the arched bridges internal forces of arbitrary shape using the elastic-plastic work of the material. Three equilibrium differential equations, which are solved analytically, and an example of calculating an arch on a concentrated force action are presented. A simplified model of the cracks formation and plastic deformations in reinforced concrete round arches is considered in [2]. The solution was obtained on the basis of the additional energy functional and the generalized Griffith criterion of the crack propagation. Comparison of numerical solutions with experimental results is performed. The papers [3], [4] are devoted to the numerical and experimental study of brick arches. In [3] the arch is represented by a system of rigid blocks connected by three links, and combinatorial analysis was used to determine the hinges location at small displacements of the supports. In article [5] investigates the stone arches destruction mechanisms under the concentrated forces action and notes the importance of taking into account the possibility of occurrence of shifts between the rigid blocks.

A number of papers are devoted to optimizing the arches shapes [6], [7]. In article [6] optimizes the underground concrete arch shape in order to reduce bending stresses. The arch is calculated using a nonlinear finite element model. The arch center line is approximated by a Bezier curve with three degrees of freedom. The optimal parameters are determined using a genetic algorithm. The masonry arches

destruction mechanisms and concrete blocks arch are largely similar. Numerous studies have been devoted to the study of arched masonry bridges work [8]–[11]. The article [12] provides an overview of research on reinforcing brick arches methods with composite materials. In particular, the use of fiber-reinforced cement matrix (FRCM) materials to reinforce brick arches is explored in [13]. The article presents numerical and experimental studies of arches reinforced with such materials. Arches are modeled with a rigid blocks set. In a number of works, volumetric finite elements are used to calculate stone and concrete structures [11], [14], [15]. In [11], it is presents the combined finite-discrete element method (FDEM) application to the analysis of three-dimensional stone structures from dry stone. The article [16] presents experimental and numerical studies results of a multi-span arched masonry bridge response to vertical static loads. In [17], a two-phase strategy for the numerical simulation of the arched bridges stone destruction process is presented, in which stone blocks are represented by solid elements, and the solution was described by special finite elements. Three modes of destruction (compression, tension and shear) for masonry materials are considered. Article [18] is devoted to the masonry numerical analysis based on experimental data, where the compressible-bendable elements behavior is investigated. When calculating arched bridges, it is important to take into account shear deformations [19], [20]. The shear deformations accounting theory of the circular arches was proposed in [20]. This paper presents an analytical solution of calculating circular arches based on the logarithmic functions using. Shear deformations consideration based on stresses approximations is presented in the works [21], [22].

Based on the foregoing, we can note the relevance of the arch bridge optimal shape determining problem, which is constructed of concrete blocks. And, it is necessary to take into account the concrete nonlinear deformations and a cracking between blocks process. The study aim was to develop an arched bridge optimal shape determining method in order to ensure the compressed cross-sectional zone required size at the automobile load any position.

2 Materials and Methods

This paper considers a method of determining the arch optimal shape and cross-section dimensions, which are provide the necessary arch strength at automobile load any position, as well as a given minimum compressed zone height of the any cross-section along the arch length (Fig. 1).

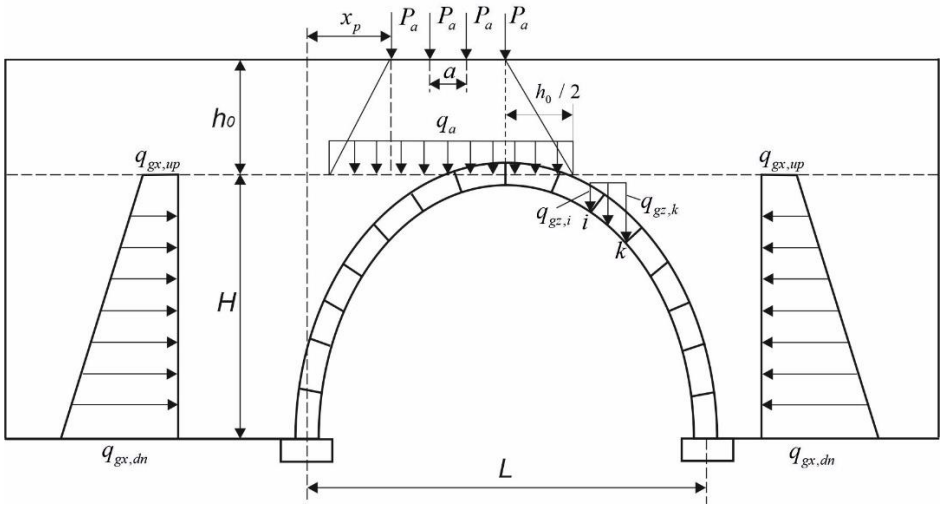

Fig. 1 - A concrete blocks arch in the ground

The concrete stress-strain diagram of the arch is presented in the piecewise-broken curve form, which does not take into account the tensile concrete stresses (Fig. 2).

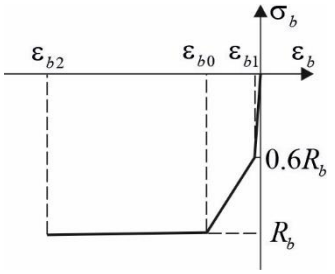

Fig. 2 - The concrete stress-strain diagram

Such a diagram is used because tensile stresses cannot arise in the concrete blocks joints sections. In the sections between the joints, for the safety margin, the tensile concrete stresses will also be neglected. With this approach, the arch calculation will not depend on the length of the concrete blocks and the number of joints.

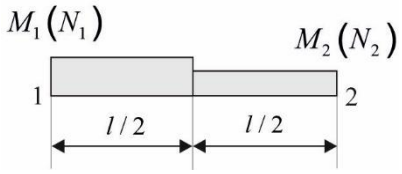

Fig. 3 - Bending moments and longitudinal forces approximations along a finite element length

To solve the problem with a physically nonlinear formulation, we will use a step loading method and possible stress states principle. For an arbitrary load step, variation of the additional deformations' energy increment $\delta(\Delta\Pi_i)$ is zero.

$$\delta(\Delta\Pi_i) = \int_V (\varepsilon_i + \delta(\Delta\varepsilon_i))\delta(\Delta\sigma_i)\mathrm{dV} = 0. \quad (1)$$

ε_i, $\Delta\varepsilon_i$ are the current deformations and deformations increments at a loading step; $\Delta\sigma_i$ is the stresses increments, which must satisfy the equilibrium equations at loading step; V is subject area. The deformations and stresses increments, at an arbitrary point, at each step are interconnected by the deformation tangent modulus $E_i^t(\varepsilon_i)$:

$$\Delta\sigma_i = E_i^t(\varepsilon_i)\Delta\varepsilon_i. \quad (2)$$

Substituting (2) into (1), we get:

$$\delta(\Delta\Pi_i) = \int_v E_i^t(\varepsilon_i)(\varepsilon_i + \delta(\Delta\varepsilon_i))\delta(\Delta\varepsilon_i)\mathrm{dV} = 0. \quad (3)$$

From expression (3) it follows that the additional strain energy increment will have the following form:

$$\Delta\Pi_i = \int_v \left(E_i^t(\varepsilon_i)\varepsilon_i\Delta\varepsilon_i + \frac{1}{2}E_i^t(\varepsilon_i)\Delta\varepsilon_i^2 \right)\mathrm{dV}. \quad (4)$$

Let us calculate the additional energy deformations increment of a rod finite element. The strains increments are determined according to the straight normal hypothesis:

$$\Delta\varepsilon_i = \Delta\varepsilon_{0i} - z\Delta\chi_i. \quad (5)$$

$\Delta\varepsilon_{0i}$ is the increment of midline deformation; $\Delta\chi_i$ is axis curvature increment. Substituting (5) into (4), we get:

$$\Delta\Pi_{i,k} = \int_0^{l_k}\int_{-h/2}^{h/2} b(\varepsilon_{0i} - z\chi_i)\Delta\sigma_i\mathrm{dz}\mathrm{dx} + \frac{1}{2}\int_0^{l_k}\int_{-h/2}^{h/2} bE_i^t(\varepsilon_i)(\Delta\varepsilon_{0i}^2 - 2z\Delta\varepsilon_{0i}\Delta\chi_i + \Delta\chi_i^2)\mathrm{dz}\mathrm{dx}. \quad (6)$$

Let us introduce notation for the following integrals:

$$EA^t = \int_{-h/2}^{h/2} bE_i^t(\varepsilon_i)\mathrm{dz},\ ES^t = \int_{-h/2}^{h/2} bE_i^t(\varepsilon_i)z\mathrm{dz},\ EI^t = \int_{-h/2}^{h/2} bE_i^t(\varepsilon_i)z^2\mathrm{dz}. \quad (7)$$

Integrals (7) are calculated numerically using the concrete stress-strain diagram (Fig. 2) by the trapezia method. Considering (7), the internal forces increments in the section are determined by the following formulas:

$$\Delta N_i = \int_{-h/2}^{h/2} b\Delta\sigma_i \mathrm{d}z = \int_{-h/2}^{h/2} bE_i^t\left(\varepsilon_i\right)\left(\Delta\varepsilon_{0i} - z\Delta\chi_i\right)\mathrm{d}z = \Delta\varepsilon_{0i}EA^t - \Delta\chi_{ii}ES^t, \tag{8}$$

$$\Delta M_i = -\int_{-h/2}^{h/2} b\Delta\sigma_i z\mathrm{d}z = -\int_{-h/2}^{h/2} bE_i^t\left(\varepsilon_i\right)\left(z\Delta\varepsilon_{0i} - z^2\Delta\chi_i\right)\mathrm{d}z = -\Delta\varepsilon_{0i}ES^t + \Delta\chi_{ii}EI^t. \tag{9}$$

From expressions (8), (9) we obtain

$$\Delta\varepsilon_{0i} = \frac{\Delta N_i EI^t + \Delta M_i ES^t}{EA^t EI^t - ES^{t2}},\ \Delta\chi_i = \frac{\Delta N_i ES^t + \Delta M_i EA^t}{EA^t EI^t - ES^{t2}}. \tag{10}$$

Substituting (10) into (6), we get

$$\Delta\Pi_{i,\mathrm{k}} = \int_0^{l_k}\left(\varepsilon_{0i}\Delta N_i + \chi_i\Delta M_i\right)\mathrm{d}x + \frac{1}{2}\int_0^{l_k}\left(\frac{EI^t\Delta N_i^{\,2}}{EI^tEA^t - ES^{t2}} + \frac{EA^t\Delta M_i^{\,2}}{EI^tEA^t - ES^{t2}} + \frac{2ES^t\Delta M_i\Delta N_i}{EI^tEA^t - ES^{t2}}\right)\mathrm{d}x. \tag{11}$$

Let us introduce the vectors of unknown nodal forces and its increments for a finite element:

$$\mathbf{S}_{i,k} = \begin{Bmatrix} N_{i,1} \\ M_{i,1} \\ N_{i,2} \\ M_{i,2} \end{Bmatrix},\ \Delta\mathbf{S}_{i,k} = \begin{Bmatrix} \Delta N_{i,1} \\ \Delta M_{i,1} \\ \Delta N_{i,2} \\ \Delta M_{i,2} \end{Bmatrix}. \tag{12}$$

To approximate the forces and moments along the finite element length, we will use piecewise-constant approximations (Fig. 3). Such approximations make it possible to simplify the flexibility matrix elements calculations of a finite element. In this case, the global flexibility matrix will have a block-diagonal shape and will be easily reversible. The expression (11) can be written in matrix form:

$$\Delta\Pi_{i,\mathrm{k}} = \frac{1}{2}\Delta\mathbf{S}_{i,k}^{\mathrm{T}}\mathbf{D}_{i,k}^t\Delta\mathbf{S}_{i,k} + \boldsymbol{\varepsilon}_{i,\mathrm{k}}^{\mathrm{T}}\Delta\mathbf{S}_{i,k}, \tag{13}$$

$$\mathbf{D}_{i,k}^t = \frac{l_k}{2}\begin{bmatrix} \frac{EI_1^{\,t}}{ER_1^{\,t}} & \frac{ES_1^{\,t}}{ER_1^{\,t}} & 0 & 0 \\ \frac{ES_1^{\,t}}{ER_1^{\,t}} & \frac{EA_1^{\,t}}{ER_1^{\,t}} & 0 & 0 \\ 0 & 0 & \frac{EI_2^{\,t}}{ER_2^{\,t}} & \frac{ES_2^{\,t}}{ER_2^{\,t}} \\ 0 & 0 & \frac{ES_2^{\,t}}{ER_2^{\,t}} & \frac{EA_2^{\,t}}{ER_2^{\,t}} \end{bmatrix},\ \boldsymbol{\varepsilon}_{i,k} = \begin{Bmatrix} \varepsilon_{i,1} \\ \chi_{i,1} \\ \varepsilon_{i,2} \\ \chi_{i,2} \end{Bmatrix}, \tag{14}$$

$$ER_1^{/} = EI_1^{\,t}EA_1^{\,t} - ES_1^{\,t2},\ ER_2^{/} = EI_2^{\,t}EA_2^{\,t} - ES_2^{\,t2}. \tag{15}$$

EA_1^t, ES_1^t, EI_1^t, EA_2^t, ES_2^t, EI_2^t are the finite element stiffness parameters for the beginning and end sections, calculated by formulas (7). Matrix (14) was obtained for the case when the cross section is constant along the finite element length.

If the section width or height changes along the element length, then the second integral in (11), which determines the tangent matrix elements, is calculated numerically using the trapezia formula. Divide the finite element into 2*n* equal segments $\Delta l_k = l_k / 2n$. Let us denote the shear stiffness generalized parameters of the section at an arbitrary point of the finite element:

$$EA_j^t = \int_{-h_j/2}^{h_j/2} b_j E_i^t\left(\varepsilon_{i,j}\right)\mathrm{d}z,\ ES_j^t = \int_{-h_j/2}^{h_j/2} b_j E_i^t\left(\varepsilon_{i,j}\right)z\mathrm{d}z,\ EI_j^t = \int_{-h_j/2}^{h_j/2} b_j E_i^t\left(\varepsilon_{i,j}\right)z^2\mathrm{d}z,$$
$$ER_j^t = EI_j^t EA_j^t - ES_j^{t2}. \tag{16}$$

b_j, h_j are the section dimensions at point *j*. Deformations $\varepsilon_{i,j}$ are determined depending on which finite element half of the length the section j is located:

$$\begin{cases} \varepsilon_{i,j} = \varepsilon_{i,1} - z\chi_{i,1}, & j = 1,..,n+1, \\ \varepsilon_{i,j} = \varepsilon_{i,2} - z\chi_{i,2}, & j = n+1,..,2n+1. \end{cases} \tag{17}$$

Let us introduce the tangent matrix $\mathbf{D}_{i,k}^t$ elements notation:

$$d_{1,1} = \sum_{j=2}^{n} \frac{EI_j^t}{ER_j^t} + \frac{EI_1^t}{2ER_1^t} + \frac{EI_{n+1}^t}{2ER_{n+1}^t},\quad d_{2,2} = \sum_{j=2}^{n} \frac{EA_j^t}{ER_j^t} + \frac{EA_1^t}{2ER_1^t} + \frac{EA_{n+1}^t}{2ER_{n+1}^t},$$
$$d_{1,2} = d_{2,1} = \sum_{j=2}^{n} \frac{ES_j^t}{ER_j^t} + \frac{ES_1^t}{2ER_1^t} + \frac{ES_{n+1}^t}{2ER_{n+1}^t},$$
$$d_{3,3} = \sum_{j=n+2}^{2n} \frac{EI_j^t}{ER_j^t} + \frac{EI_{n+1}^t}{2ER_{n+1}^t} + \frac{EI_{2n+1}^t}{2ER_{2n+1}^t},\quad d_{4,4} = \sum_{j=n+2}^{2n} \frac{EA_j^t}{ER_j^t} + \frac{EA_{n+1}^t}{2ER_{n+1}^t} + \frac{EA_{2n+1}^t}{2ER_{2n+1}^t},$$
$$d_{3,4} = d_{4,3} = \sum_{j=n+2}^{2n} \frac{ES_j^t}{ER_j^t} + \frac{ES_{n+1}^t}{2ER_{n+1}^t} + \frac{ES_{2n+1}^t}{2ER_{2n+1}^t}. \tag{18}$$

The final matrix $\mathbf{D}_{i,k}^t$ expression, for the case of a variable cross section, is as follows:

$$\mathbf{D}_{i,k}^t = \Delta l_k \begin{bmatrix} d_{1,1} & d_{1,2} & 0 & 0 \\ d_{1,2} & d_{2,2} & 0 & 0 \\ 0 & 0 & d_{3,3} & d_{3,4} \\ 0 & 0 & d_{3,4} & d_{4,4} \end{bmatrix}. \tag{19}$$

The corresponding global tangent matrix $\mathbf{D}_i^t$ and vector $\boldsymbol{\varepsilon}_i$ for the whole system are formed from matrices $\mathbf{D}_{i,k}^t$ and vectors $\boldsymbol{\varepsilon}_{i,k}$. Then, for the whole system, we obtain the following expression for the increment of additional energy of the deformations:

$$\Delta\Pi_i = \frac{1}{2}\Delta\mathbf{S}_i^{\mathrm{T}}\mathbf{D}_i^t\Delta\mathbf{S}_i + \boldsymbol{\varepsilon}_i^{\mathrm{T}}\Delta\mathbf{S}_i. \tag{20}$$

In accordance with the possible stress states principle, the forces and moments increments must satisfy the equilibrium equations. Such equations for nodes can be obtained using the possible displacements principle [21]–[25]. The nodes vertical and horizontal displacements are taken as possible displacements. For the whole system, the equilibrium equations can be written in the following matrix form:

$$\mathbf{L}\Delta\mathbf{S}_i + \Delta\mathbf{P}_i = 0. \tag{21}$$

The global equilibrium matrix $\mathbf{L}$ is formed from equilibrium matrices $\mathbf{L}_k$ of finite elements.

$$\mathbf{L}_k = \begin{bmatrix} \frac{-\cos\alpha}{2} & \frac{\sin\alpha}{l_k} & \frac{-\cos\alpha}{2} & \frac{-\sin\alpha}{l_k} \\ \frac{-\sin\alpha}{2} & \frac{-\cos\alpha}{l_k} & \frac{-\sin\alpha}{2} & \frac{\cos\alpha}{l_k} \\ \frac{\cos\alpha}{2} & \frac{-\sin\alpha}{l_k} & \frac{\cos\alpha}{2} & \frac{\sin\alpha}{l_k} \\ \frac{\sin\alpha}{2} & \frac{\cos\alpha}{l_k} & \frac{\sin\alpha}{2} & \frac{-\cos\alpha}{l_k} \end{bmatrix},\ \cos\alpha = \frac{x_2 - x_1}{l_k},\ \sin\alpha = \frac{y_2 - y_1}{l_k}. \tag{22}$$

Note that the matrix $\mathbf{L}$ is geometric and does not change during step loading. The load vector $\Delta\mathbf{P}_i$ is formed from the forces concentrated in the nodes and the loads distributed over the finite element. For that we must calculate the load work at possible displacements of the nodes.

Using the Lagrange multiplier method, we add the nodes equilibrium equations (21) with the functional (20). We get the following advanced functional:

$$\Delta\Pi_i = \frac{1}{2}\Delta\mathbf{S}_i^{\mathrm{T}}\mathbf{D}_i^t\Delta\mathbf{S}_i + \boldsymbol{\varepsilon}_i^{\mathrm{T}}\Delta\mathbf{S}_i + \mathbf{w}_i^{\mathrm{T}}\left(\mathbf{L}\Delta\mathbf{S}_i + \Delta\mathbf{P}_i\right). \tag{23}$$

The Lagrange multipliers vector consists of the nodes displacements values:

$$\mathbf{w}_i^{\mathrm{T}} = \left(u_1 \quad w_1 \quad u_2 \quad w_2 \quad \ldots \quad \ldots \quad u_n \quad w_n\right). \tag{24}$$

Equating the functional derivatives with respect to vectors $\Delta\mathbf{S}_i^{\mathrm{T}}$ and $\mathbf{w}_i^{\mathrm{T}}$, we obtain the linear algebraic equations system:

$$\begin{aligned} &\mathbf{D}_i^t\Delta\mathbf{S}_i + \boldsymbol{\varepsilon}_i + \mathbf{L}^{\mathrm{T}}\mathbf{w}_i = 0, \\ &\mathbf{L}\Delta\mathbf{S}_i + \Delta\mathbf{P}_i = 0. \end{aligned} \tag{25}$$

Let us express from the first equation the forces increment vector

$$\Delta\mathbf{S}_i = -\mathbf{D}_i^{t^{-1}}\boldsymbol{\varepsilon}_i - \mathbf{D}_i^{t^{-1}}\mathbf{L}^{\mathrm{T}}\mathbf{w}_i. \tag{26}$$

The matrix $\mathbf{D}_i^t$ is block-diagonal and easily inverted. Let us introduce notation of the matrix product:

$$\mathbf{K}_i = \mathbf{L}\mathbf{D}_i^{t^{-1}}\mathbf{L}^{\mathrm{T}}. \tag{27}$$

From the second equation (25) we obtain the resolving system of nonlinear algebraic equations

$$\mathbf{K}_i\mathbf{w}_i = \Delta\mathbf{P}_i - \mathbf{D}_i^{t^{-1}}\boldsymbol{\varepsilon}_i. \tag{28}$$

At each loading step, we will perform iterative refinement according to the Newton - Raphson scheme. We will use the following calculation algorithm with given automobile position:

1. Calculate matrix $\mathbf{L}$ and vector $\mathbf{P}$; $\boldsymbol{\varepsilon}_i = 0$; $\mathbf{S}_i = 0$;
2. Set the number of load steps *n* and required accuracy $\left[Ex\right]$ [%]; $i = 0$.
3. Begin load cycle; accept $i = i + 1$; $k = 0$.
4. Accept $\Delta\overline{\mathbf{S}}_i = 0$; $\Delta\mathbf{P}_i = \frac{1}{n}\mathbf{P}$.
5. Begin cycle of iterative refinement; accept $k = k + 1$.
6. Calculate matrix $\mathbf{D}_i^t$, $\mathbf{D}_i^{t^{-1}}$, $\mathbf{K}$.
7. Calculate equations system (24); calculate $\mathbf{w}_i$.
8. From (22) calculate $\Delta\mathbf{S}_i$; $\mathbf{S}_i = \mathbf{S}_i + \Delta\mathbf{S}_i$.
9. Using (10), calculate $\Delta\boldsymbol{\varepsilon}_i$; $\boldsymbol{\varepsilon}_i = \boldsymbol{\varepsilon}_i + \Delta\boldsymbol{\varepsilon}_i$.
10. Using in (8) and (9) secant modulus of deformations; calculate $\overline{\mathbf{S}}_i$.
11. Calculate $\Delta\overline{\mathbf{S}}_k = \mathbf{S}_i - \overline{\mathbf{S}}_i$; $\Delta\overline{\mathbf{S}}_i = \Delta\overline{\mathbf{S}}_i + \Delta\overline{\mathbf{S}}_k$.
12. Calculate $\Delta\overline{\mathbf{P}}_i = \mathbf{L}\Delta\overline{\mathbf{S}}_i$ and accuracy $Ex\left(\Delta\mathbf{P}_i\right) = 100\dfrac{\sqrt{\sum_{j=1}^{n_d}\left(\Delta P_{i,j} - \Delta\overline{P}_{i,j}\right)^2}}{\sqrt{\sum_{j=1}^{n_d}\Delta P_{i,j}{}^2}}$.
13. If $Ex\left(\Delta\mathbf{P}_i\right) > \left[Ex\right]$, then calculate $\Delta\mathbf{P}_i = \Delta\mathbf{P}_i - \mathbf{L}\Delta\overline{\mathbf{S}}_i$; $\mathbf{S}_i = \overline{\mathbf{S}}_i$ and go to 5.
14. If $Ex\left(\Delta\mathbf{P}_i\right) \le \left[Ex\right]$, then end of iterative refinement, go to 3.
15. End of load cycle.

The resulting bending moments are used to calculate the shear forces of finite elements:

$$Q_k = \frac{M_2 - M_1}{l_k}. \tag{29}$$

Next, the check is performed of a possible shift in the cross sections where the concrete blocks joints are located:

$$|Q_k| \le k_{fr} |N_1|, \quad |Q_k| \le k_{fr} |N_2|. \tag{30}$$

k_{fr} is the friction coefficient of concrete on concrete; N_1, M_1, N_2, M_2 are the internal forces at the finite element beginning and end. If conditions (30) are not done, then a shift of concrete blocks relative to each other is possible and it is necessary to make adjustments to the design scheme.

At each node of the arch, the eccentricity modulus of the longitudinal force and the required section height are calculated, which provides the compressed zone will be equal to half the height (with a linear stress diagram in the compressed zone):

$$e_i = \left| \frac{M_i}{N_i} \right|, \; h_i^s = 3 \cdot e_i. \tag{31}$$

Calculations have shown that the maximum compressive stresses are far from the limiting value; therefore, the stress diagram in the compressed zone is practically linear. Nonlinearity of deformations is associated with the exclusion of the stretched concrete zone from the work.

The required heights of the arch cross sections will be determined using the following iterative algorithm:

1. For each arch node, we set the initial value of the section height $h_i = h_{\min}$.
2. Refinement h_i cycle.
3. Set $h_i^{iter} = h_i$.
4. Begin cycle on x_p (рис.1) from 0 to $\left(\frac{L}{2} - \frac{a_x}{2} \right)$ with step 0.1 m.
5. We perform the arch calculation according to the algorithm given above.
6. For each arch node, we calculate h_i^s (31).
7. If $h_i^s > h_i^{iter}$, then $h_i^{iter} = h_i^s$.
8. End cycle on x_p.
9. For each arch node, we calculate $h_i = \left(\frac{10000 \cdot h_i^{iter} + h_i}{10000} \right) \ge h_{\min}$.
10. Rounding h_i to 5 cm.
11. Go to 2.

Calculations have shown that the process of refining the cross-section heights converges in no more than 15 iterations. As a result of the calculation, for each node, the maximum eccentricities of the longitudinal force and the required section height are determined. These heights will ensure the compressed zone value at least half of the cross section at any automobile load position.

3 Results and Discussion

As an example, let us determine the optimal parameters of the pointed arch (Fig. 4), when it is given span and the soil backfill height (Fig. 1). In this case, the compressed zone minimum height should be at least half the arch section height. The arch supports were taken pinched. But the supports have the ability to tear off, since the concrete tensile work is not taken into account. Calculation of the arch height, which depend on the span length and the half-arch arc radius, are shown in Fig. 4. The all data for the calculation are given in Table 1. The arch was divided along the length into 16 finite elements (Fig. 5).

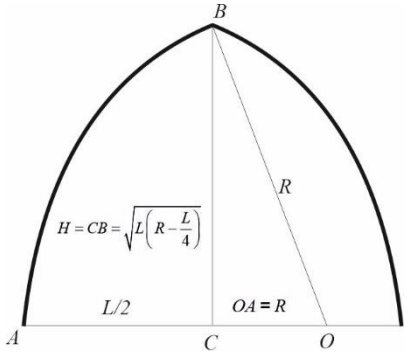

Fig. 4 - Geometry of pointed arch

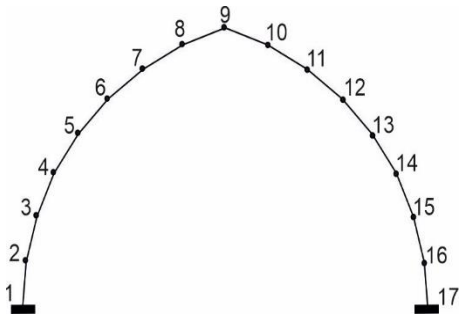

Fig. 5 - Arch nodes numbering

Table 1. Arch calculation data

Denotation	Dimension	Value	Parameter
h_0	m	2.0	Backfill height from the arch top
φ_{gr}	degree	35	Angle of internal soil friction
γ_{gr}	kN/m^3	17.7	Soil volume weight
a	m	1.2	Distance between vehicle axles
P_a	kN	250	Vehicle axle load
a_x	m	3.6	Load length from vehicle
a_y	m	2.7	Load width from vehicle
L	m	12	Arch span
B	m	0.5	Arch width
$h_{\min}$	m	Need to assign	The minimum height of the arch cross section
R	m	Calculated	Half-arch arc radius
H	m	$\sqrt{L(L-R/4)}$	Arch height

Vertical and horizontal loads from the vehicle and the ground (Fig. 1) are determined by the following formulas:

$$q_a = \frac{1.2 \cdot B \cdot P_a}{(h_0 + a_x)(h_0 + a_y)}, \; q_{gz,i} = 1.1 \cdot \gamma_{gr} (H + h_0 - z_i) \cdot B. \tag{32}$$

$$q_{qx,up} = 1.1 \cdot \gamma_{gr} h_0 \cdot tg^2 \left(45 - \frac{\varphi_{gr}}{2}\right) B, \; q_{qx,dn} = 1.1 \cdot \gamma_{gr} (H + h_0) \cdot tg^2 \left(45 - \frac{\varphi_{gr}}{2}\right) B. \tag{33}$$

To these loads is added the load from the arch's own weight.

The parameters of the compressed concrete deformation diagram were taken as follows: $\varepsilon_{b1} = -0.000314$, $\varepsilon_{b0} = -0.002$, $\varepsilon_{b2} = -0.0035$, $R_b = 17000\ kN/m^2$ (Fig. 2).

Fig. 6 shows the most optimal arch with the minimum weight ($h_{\min} = 0.4\,m$). Fig. 7, for comparison, shows an arch whose weight is slightly greater, but it has the different arc radius.

Table 2 shows the weights of arches at the various values R and $h_{\min}$.

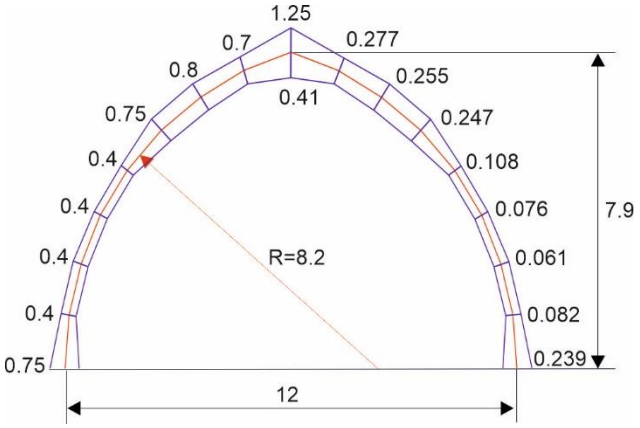

Fig. 6 - Arch with the minimum weight of 17.03 tons: on the left side the blocks section heights are indicated; on the right side the maximum eccentricities of the longitudinal force (in meters) are indicated

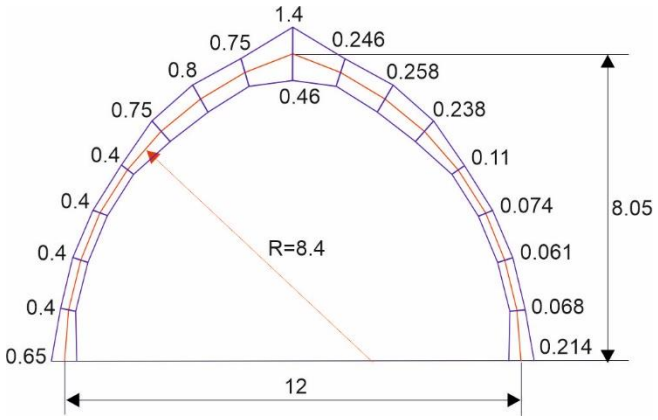

Fig. 7 - Arch weight of 17.47 tons: on the left side the blocks section heights are indicated; on the right side the maximum eccentricities of the longitudinal force (in meters) are indicated

Table 2. Arch weight in tons depending on geometric parameters

$\left(R-\frac{L}{2}\right)$[m]	$h_{\min}$ [m]			
	0.3	0.4	0.5	0.6
1.9		18.932	18.240	**19.105**
2.0		18.248	**18.162**	19.291
2.1		17.906	18.255	19.391
2.2		**17.032**	18.394	19.481
2.3	18.001	17.559	18.353	20.030
2.4	**17.470**	17.470	18.623	20.219
2.5	17.825	17.914	18.983	

Analyzing the calculation results given in Table 2, we note that each minimum section height corresponds to a certain arc radius and the arch height, when the arch has the least weight. Moreover, the lower the minimum section height, the greater the arch required height. Empty cells of Table 2 correspond to arches that cannot withstand the applied loads or are non-optimal.

To compare the results, the arch (Fig. 6) was calculated using the proposed method and the LIRA-SAPR program for the case when the automobile load is located symmetrically relative to the arch top. In the LIRA-SAPR program, there are no finite elements of variable cross-section along the length, therefore, such finite elements were replaced by two finite elements with constant, step-changing cross sections. The internal forces values and eccentricities obtained by the proposed method and by the LIRA-SAPR program are presented in Table 3. The nodes longitudinal forces obtained with the LIRA-SAPR program were determined as the average value of the longitudinal forces in the finite elements adjacent to the node.

Table 3. Internal forces and moments at the arch shown in Fig. 6

Node	Proposed method			LIRA-SAPR			
	N [kN]	*M* [kNm]	$e=\left\|\frac{M}{N}\right\|[m]$	*N* [kN]	*N*cp [kN]	*M* [kNm]	$e=\left\|\frac{M}{N_{\text{cp}}}\right\|[m]$
1	-380.97	77.11	0.202	-371.39	-371.39	67.8	0.183
2	-361.90	15.5	0.043	-371.39 -363.95	-367.67	13.0	0.035
3	-366.84	-16.62	0.045	-363.95 -345.08	-354.52	-17.7	0.050
4	-324.18	-21.66	0.067	-345.08 -319.59	-332.60	-21.5	0.065
5	-316.12	-5.65	0.018	-319.59 -293.85	-306.72	-4.28	0.014
6	-269.19	24.26	0.090	-256.97 -288.51	-272.74	26.8	0.098
7	-246.44	47.35	0.192	-256.97 -222.77	-239.87	50.73	0.211
8	-200.98	40.13	0.200	-222.77 -200.78	-211.78	44.18	0.209
9	-202.58	-7.54	0.037	-200.78	-200.78	-2.86	0.014

Note that the longitudinal forces values of the two methods differ insignificantly. The bending moments values differ within 15%. The exception is the moments at the arch top, where the difference is most significant, but the moment magnitude at a given node is an order of magnitude less than at other nodes. In general, the calculation results of the two programs agree with satisfactory accuracy. When we calculate with the LIRA-SAPR program, 2000 steps were specified for the load, since the results turned out to be very sensitive in the step size. When calculating according to the proposed method for the convergence of the solution, it was enough to use 10 steps on the load.

To assess the arch safety margin, calculations were performed with a gradual increase in the automobile load value P_a. Three positions of the load were considered: 1 – symmetrically relative to the arch top; 2 – the load is shifted 1.2 meters to the left from the top; 3 – the load is shifted 2.4 meters to the left of the top. The results are shown in Fig. 8-9.

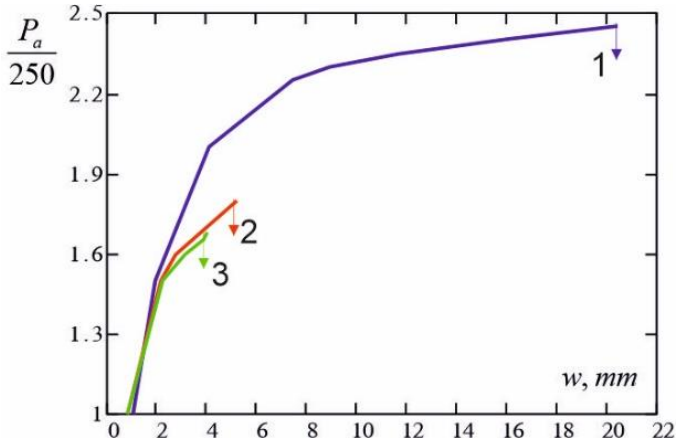

Fig. 8 - Displacements of the arch top (Fig. 6) with an increase of the automobile load until the arch destruction: 1 - the load is located symmetrically; 2 - load with a shift of 1.2 m from the top; 3 - load with a shift of 2.4 m from the arch top

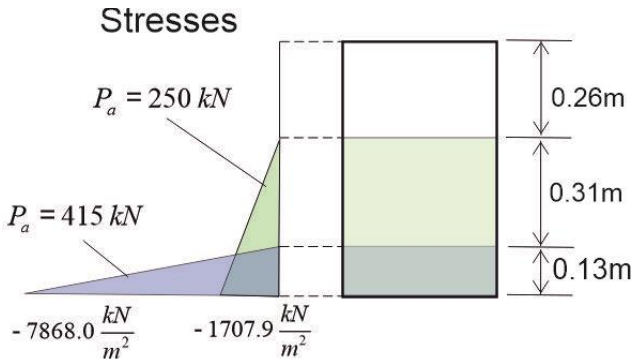

Fig. 9 - Stresses in the arch section at node 8 (Fig. 6), the automobile load is applied with a shift of 2.4 m from the arch top

If the automobile load is located symmetrically with respect to the arch top, then the breaking load exceeds the calculated one by about 2.4 times. At the most disadvantageous position of the load $P_a = 415\,kN$ when it is with an offset of 2.4 meters from the symmetry axis, the breaking load exceeds the design load by about 1.6 times. In this case, the maximum edge stresses of concrete are less than half the compressive concrete strength. Before crash, the compressed concrete zone at node 8 decreases to 1/5 of the section height (Fig. 9), and the vertical displacements of the arch top increase approximately 4 times (Fig. 8). The arch nodes displacements are small, and by their magnitude it is difficult to determine the destruction proximity of the arch structure. Therefore, it can be noted that the arch structure made of the concrete blocks is susceptible to brittle crash, without visible increasing of deformations. Nevertheless, the destructive automobile load is 1.6 times higher than the calculated one, which provides a certain safety margin of the arch. The graphs in Fig. 6 demonstrate the significant influence of the automobile load location on value, which destroys the arch. Note that the required friction coefficient between the blocks, which prevents the blocks from shifting relative to each other, does not exceed 0.5.

If it is necessary to provide the arch greater safety margin, then calculations should be performed with an increase in the value of the minimum height of the section compressed zone, for example, to the value $(0.6-0.7)h$.

4 Conclusions

1. The method is proposed for optimal parameters determining of an underground arch made of concrete blocks under the action of an automobile load, a load from the soil and its own weight. The optimal parameters of the arch are determined on the condition that the compressed zone minimum height is more than half of the arch section at any automobile load position.
2. Calculation of the arch is carried out by the finite element method based on the approximation of forces and moments. For the solution, the possible stress states principle, written on increments form, and the possible displacements principle to obtain the equilibrium arch nodes equations are used. The compressed concrete stress-strain diagram is assumed to be nonlinear. The tensile concrete work is not considered.
3. The proposed calculation method makes it possible to determine the automobile load limiting value for the arch and to estimate the arch bridge safety margin.
4. Optimum geometric parameters have been determined for an arched bridge with the span of 12 meters. The destructive automobile load value is determined. For the design load the obtained internal forces are compared with the forces calculated by the program based on the finite element method in displacements.

References

1. Audenaert, A., Fanning, P., Sobczak, L., Peremans, H. 2-D analysis of arch bridges using an elasto-plastic material model. Engineering Structures. 2008. 30(3). Pp. 845–855. DOI:10.1016/j.engstruct.2007.05.018.
2. Amorim, D.L.N.D.F., Proença, S.P.B., Flórez-López, J. A model of fracture in reinforced concrete arches based on lumped damage mechanics. International Journal of Solids and Structures. 2013. 50(24). Pp. 4070–4079. DOI:10.1016/j.ijsolstr.2013.08.012.
3. Galassi, S., Misseri, G., Rovero, L., Tempesta, G. Failure modes prediction of masonry voussoir arches on moving supports. Engineering Structures. 2018. 173(July). Pp. 706–717. DOI:10.1016/j.engstruct.2018.07.015.
4. Gattesco, N., Boem, I., Andretta, V. Experimental behaviour of non-structural masonry vaults reinforced through fi bre-reinforced mortar coating and subjected to cyclic horizontal loads. Engineering Structures. 2018. 172(December 2017). Pp. 419–431. DOI:10.1016/j.engstruct.2018.06.044.
5. Beatini, V., Royer-Carfagni, G., Tasora, A. Modeling the shear failure of segmental arches. International Journal of Solids and Structures. 2019. 158. Pp. 21–39. DOI:10.1016/j.ijsolstr.2018.08.023.
6. Houšt', V., Eliáš, J., Miča, L. Shape optimization of concrete buried arches. Engineering Structures. 2013. 48. Pp. 716–726. DOI:10.1016/j.engstruct.2012.11.037.
7. Kimura, T., Ohsaki, M., Fujita, S., Michiels, T., Adriaenssens, S. Shape optimization of no-tension arches subjected to in-plane loading. Structures. 2020. 28(August). Pp. 158–169. DOI:10.1016/j.istruc.2020.08.053.
8. Misseri, G., Justin, M., Rovero, L. Experimental and numerical investigation of the collapse of pointed masonry arches under quasi-static horizontal loading. Engineering Structures. 2018. 173(October 2017). Pp. 180–190. DOI:10.1016/j.engstruct.2018.06.009.
9. Pulatsu, B., Erdogmus, E., Lourenço, P.B. Comparison of in-plane and out-of-plane failure modes of masonry arch bridges using discontinuum analysis. Engineering Structures. 2019. 178(August 2018). Pp. 24–36. DOI:10.1016/j.engstruct.2018.10.016.
10. Scozzese, F., Ragni, L., Tubaldi, E., Gara, F. Modal properties variation and collapse assessment of masonry arch bridges under scour action. Engineering Structures. 2019. 199(September). Pp. 109665. DOI:10.1016/j.engstruct.2019.109665.
11. Smoljanović, H., Živaljić, N., Nikolić, Ž., Munjiza, A. Numerical analysis of 3D dry-stone masonry structures by combined finite-discrete element method. International Journal of Solids and Structures. 2018. 136–137. Pp. 150–167. DOI:10.1016/j.ijsolstr.2017.12.012.
12. Zampieri, P., Simoncello, N., Tetougueni, C.D., Pellegrino, C. Review article A review of methods for strengthening of masonry arches with composite materials. Engineering Structures. 2018. 171(December 2017). Pp. 154–169. DOI:10.1016/j.engstruct.2018.05.070.
13. Zampieri, P., Simoncello, N., Gonzalez-libreros, J., Pellegrino, C. Evaluation of the vertical load

capacity of masonry arch bridges strengthened with FRCM or SFRM by limit analysis. Engineering Structures. 2020. 225(July). Pp. 111135. DOI:10.1016/j.engstruct.2020.111135.
14. Dmitriev, A., Lalin, V., Novozhilov, Y., Mikhalyuk, D. Simulation of Concrete Plate Perforation by Coupled Finite Element and Smooth Particle Hydrodynamics Methods. Construction of Unique Buildings and Structures. 2020. 92(9207). DOI:10.18720/CUBS.92.7.
15. Ribeiro, F., Sena-Cruz, J., Branco, F.G., Júlio, E. 3D finite element model for hybrid FRP-confined concrete in compression using modified CDPM. Engineering Structures. 2019. 190(April). Pp. 459–479. DOI:10.1016/j.engstruct.2019.04.027.
16. Zani, G., Martinelli, P., Galli, A., di Prisco, M. Three-dimensional modelling of a multi-span masonry arch bridge: Influence of soil compressibility on the structural response under vertical static loads. Engineering Structures. 2020. 221(May). Pp. 110998. DOI:10.1016/j.engstruct.2020.110998.
17. Zhao, C., Xiong, Y., Zhong, X., Shi, Z., Yang, S. A two-phase modeling strategy for analyzing the failure process of masonry arches. Engineering Structures. 2020. 212(March). Pp. 110525. DOI:10.1016/j.engstruct.2020.110525.
18. Mohireva, A., Proskurovskis, A., Belousov, N., Nazinyan, A., Glebova, E. Strength and deformability of compressed-bent masonry structures during and after fire. Construction of Unique Buildings and Structures. 2020. 92(9203). Pp. 2–6. DOI:10.18720/CUBS.92.3.
19. Thai, S., Thai, H.T., Vo, T.P., Patel, V.I. A simple shear deformation theory for nonlocal beams. Composite Structures. 2016. 183(1). Pp. 262–270. DOI:10.1016/j.compstruct.2017.03.022.
20. Pydah, A., Batra, R.C. Shear deformation theory using logarithmic function for thick circular beams and analytical solution for bi-directional functionally graded circular beams. Composite Structures. 2017. 172. Pp. 45–60. DOI:10.1016/j.compstruct.2017.03.072.
21. Tyukalov, Y.Y. Finite element model of Reisner's plates in stresses. Magazine of Civil Engineering. 2019. 5(89). Pp. 61–78. DOI:10.18720/MCE.89.6.
22. Tyukalov, Y.Y. Calculation of circular plates with assuming shear deformations. IOP Conference Series: Materials Science and Engineering. 2019. 687(3). DOI:10.1088/1757-899X/687/3/033004.
23. Tyukalov, Y.Y. Calculation of bending plates by finite element method in stresses. IOP Conference Series: Materials Science and Engineering. 2018. 451(1). DOI:10.1088/1757-899X/451/1/012046.
24. Tyukalov, Y.Y. Equilibrium finite elements for plane problems of the elasticity theory. Magazine of Civil Engineering. 2019. 91(7). Pp. 80–97. DOI:10.18720/MCE.91.8.
25. Tyukalov, Y.Y. The functional of additional energy for stability analysis of spatial rod systems. Magazine of Civil Engineering. 2017. 70(2). DOI:10.18720/MCE.70.3.